Multi-Frequency Bands Based Pole-to-Ground Fault Detection Method for MMC-Based Radial DC Distribution Systems

Changqing Yang, Shuyue Lin*, Moufa Guo*

Electrical Engineering and Automation College, Fuzhou University, Fuzhou 350108, China.

Abstract

In a small-current grounding system, the pole-to-ground fault may cause the voltage drop in the fault pole and the voltage rise in the other poles. In flexible DC distribution systems, Severe voltage variation may shorten the insulation lifetime of the equipment, which leads to great concerns on the safety issue. In addition, the existence of high transition resistance degrades the accuracy of fault detection methods, thus further affecting the reliability of the system. Therefore, it is essential to explore an advanced technology for faulty feeder detection. This study proposes a faulty feeder detection method based on the characteristics of transient zero-mode current (TZMC) in multi-frequency bands. The change rate of zero-mode voltage is applied as the protection activation criterion. Then, the characteristic matrix is constructed via computing the fuzzy entropy of TZMC in each frequency band. Finally, the faulty feeder can be identified by conducting fuzzy C-means on the characteristic matrix. This proposed method is tested through simulations on the PSCAD/EMTDC platform, which successfully demonstrates its outstanding adaptability, reliability, and accuracy.

Keywords: Faulty feeder detection; multi-frequency bands; pole-to-ground fault; radial DC distribution systems; transient zero-mode current.

1. Introduction

The modular multilevel converter (MMC)-based flexible DC distribution systems (FDCDSs) has been widely applied in distributed energy integration and power supplies due to its good output characteristics, low losses, and excellent scalability [1]-[3]. In the MMC-based FDCDSs, pole-to-ground (PTG) fault is one of the most typical faults, which may largely affect the reliability of the system [4]-[5]. In industry, the small-current grounding system is usually deployed to improve reliability [6]. However, the fault current is sometimes too weak to be detected, particularly in the scenario of PTG fault with high transition resistance. Hence, it is of great necessity to seek a highly applicable PTG fault detection technique for the FDCDSs [7].

To improve the fault detection performance in case of weak fault current, a new pattern of grounding system has been proposed in [8]. A large resistor and arrester were connected in parallel at the AC side of the transformer to achieve differential protection in the medium-voltage DC systems. However, the detection speed is limited. In [9] and [10], they analyzed the waveform characteristics of the fault transient current to detect faults, which met the speed requirements of FDCDSs. However, the setting of the protection threshold highly relies on the simulations, resulting in low adaptability and applicability. In [11], a fault identification technique based on the fault mechanism model has been explored. It identified the faults by computing the root-mean-square value of the estimated fault current in a

* Corresponding author.
E-mail address:shuyue.lin@fzu.edu.cn(S.Lin);gmf@fzu.edu.cn(M.Guo).

http://dx.doi.org/10.1016/j.ijepes.2021.000000

lossless mirror network. But the technique is easily affected by the fault resistance, noises, and system parameters, influencing the detection accuracy. The scheme proposed in [12] covers the broad analysis under forward external faults based on line-mode and zero-mode voltages across the current-limiting reactor. However, the scheme may have selectivity issues while distinguishing between internal high-impedance faults and external low-impedance faults using the line-mode voltage. Aiming at the high impedance fault, [13] proposed a high impedance fault detection method based on improved complete ensemble empirical mode decomposition with adaptive noise, which involves the feature extraction of TZMC. But it requires multiple artificial feature extraction processes, which are more complicated and not conducive to engineering realization.

In addition, the application of machine learning technology on DC protection has been widely investigated [14]. In [15], the task of operating mode detection, topology identification, fault detection/classification, and section identification have been formulated as a set of classification problems and further solved using a random subspace sampling-based ensemble classifier technique. In [16], the multiclass support vector machine model is utilized to detect and classify different short-circuit faults in real-time operation. In [17], three neural networks were applied to identify the fault patterns by the fuzzy C-mean classification. All these methods avoid the complicated settings of the protection threshold. However, the insufficiency of the training data hinders their industrial applicability.

Hence, it is still very challenging to detect the faulty feeders effectively in the MMC-based FDCDSs. Applying the clustering algorithm may be a potential solution to overcome the above problems. Firstly, the transient zero-mode current (TZMC) frequency band characteristics will be comprehensively analyzed in internal and external fault cases. Then, a faulty feeder detection method is proposed to detect the PTG fault based on the multi-frequency bands characteristic. Finally, a radial FDCDS is constructed in PSCAD/EMTDC to validate the applicability of the proposed method. The simulation results showed that this proposed method is hardly susceptible to transition resistance, noises, fault positions, network topologies, sampling frequency, fault window length, and asynchronous sampling.

The outline is structured as follows: Section II depicts the layout of MMC-based radial FDCDSs and analyzes the frequency bands difference of the TZMC in internal and external fault cases. Section III proposes the faulty feeder detection method and introduces the corresponding algorithm, including the detection activation and fault identification strategy. Section IV and Section V test the feasibility and adaptability of the proposed method. In Section VI, the proposed scheme is compared to some existing methods. Finally, the conclusions are provided in Section VII.

2. System topology and fault analysis

2.1. Topology of a radial FDCDSs

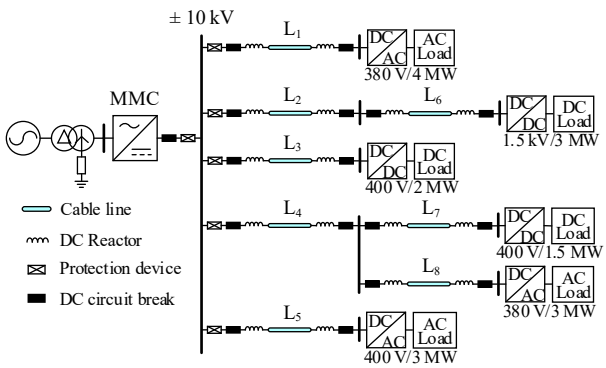

Fig. 1. The topology of radial FDCDSs

The radial FDCDS mainly consists of a half-bridge sub-module (HBSM)-MMC and radial cable lines. MMC adopts a dual closed-loop control strategy, namely the power outer loop control and the current inner loop control, to realize fast response of current and decoupling control of active and reactive power. The power outer loop control adopts constant DC voltage control [18], as shown in Fig. 1. The high-resistance grounding system is applied in the network, where 2500 Ω resistor is connected between the ground and the neutral point of the AC side of the transformer, aiming to restrict the short-circuit current [19]. The AC-DC converter adopts the topology of two-level VSC, and the double

closed-loop control strategy of power outer loop control and current inner loop control is selected. The power outer loop control adopts a constant active power control mode. The DC-DC converter comprises single-phase full-bridge controllable switching elements configured on both sides of the high-frequency AC transformer. The high-voltage side voltage of the DC transformer is controlled by the balance node in the DC distribution network, and the low-voltage side voltage is controlled by its control system. The detailed specifications are listed in Table 1.

Table 1. Parameters of radial FDCDSs

Parameter name	Parameter value
Rated voltage of AC system	110 kV
Rated voltage of DC system	±10 kV
Arm inductor	5 mH
Sub-module capacitor	23000 μF
Number of Sub-modules per arm	20
DC reactor	3 mH
Capacitance of feeder (C)	0.0583 μF/km
Inductance of feeder (L)	0.1590 mH/km
Resistance of feeder (R)	0.0139 Ω/km
Length of feeders L_1~L_8 (l)	10 km

2.2. Configuration of protection system

The protection system comprises the DC reactor, protection device, and DC circuit breaker. The protection devices are installed at the feeder terminals adjacent to the busbar and work together with the DC circuit breakers. The protection scheme is activated to collect the voltage and current data when the PTG fault occurs. The fault will be identified, and the outcome will be sent to the protection device, which then trips the corresponding DC circuit breakers.

2.3. Frequency band characteristics analysis

In an FDCDS with a small-current grounding system, there is no discharging loop for the sub-module capacitor in the converters during the PTG fault. Thus, the fault current only comes from the distributed capacitor [20]. The steady-state fault current changes slightly during the fault, making it unsuitable for the PTG fault. However, the time domain characteristic of the transient fault current is easily affected by transition resistor and load current. Therefore, analyzing the fault current in the frequency domain becomes an appropriate solution to overcome the above problem based on TZMC characteristics in multi-frequency bands. The characteristics of the internal and external faults are analyzed as follows. Note that a fault is defined to be '*internal*' to the protection device if the device is located on this fault branch. Correspondingly, this fault is defined as '*external*' to the rest of the protection devices.

2.3.1. Internal faults

When a PTG fault occurs in the line, the capacitor on one side of the π-type equivalent circuit is short-circuited, and the capacitor is quickly discharged until the current returns to zero. Therefore, to simplify the derivation process, the capacitance current of this side is set to zero [18]. The π-type equivalent circuit is displayed in Fig. 2 with a PTG fault occurring on feeder L_1. In this figure, L_r is the DC reactor, Y_1 and Y_2 are the π-type equivalent circuit admittance parameters, and $Y_3/2$ is the equivalent admittance of the DC reactor. The specific operational admittance expression is shown in (1).

$$\begin{cases} Y_1 = \dfrac{1}{Rl + Ll \cdot s} \\ Y_2 = \dfrac{Cl \cdot s}{2} \\ Y_3 = \dfrac{1}{2L_r \cdot s} \end{cases} \tag{1}$$

R, L and C are the resistance, inductance and capacitance per unit length of feeder, respectively. l is the length of the feeder.

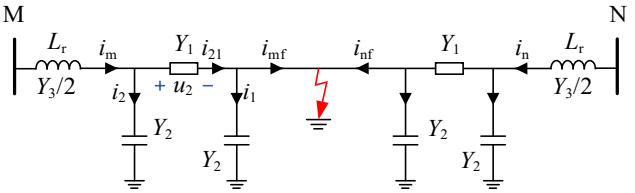

Fig. 2. The π-type equivalent circuit of internal fault

The current phasor transfer function from the grounding point to the M terminal is defined to be

$$G_m(s) = \frac{\dot{I}_{mf}(s)}{\dot{I}_m(s)} \tag{2}$$

The following equations can be obtained from Kirchhoff's law:

$$\dot{I}_2 = \dot{U}_2 \cdot Y_2 = \dot{I}_{mf} \cdot \frac{Y_2}{Y_1} \tag{3}$$

$$\dot{I}_m = \dot{I}_2 + \dot{I}_{21} = \dot{I}_{mf} \cdot \frac{Y_1 + Y_2}{Y_1} \tag{4}$$

The specific expression of the current phasor transfer function $G_m(s)$ is shown in (5), which is obtained by substituting (4) into (2):

$$G_m(s) = \frac{\dot{I}_{mf}(s)}{\dot{I}_m(s)} = \frac{Y_1}{Y_1 + Y_2} \tag{5}$$

$$f_r = \frac{\omega_r}{2\pi} \tag{6}$$

The magnitude-frequency characteristics of the current phasor transfer function $G_m(s)$ in the internal fault scenario are displayed in Fig. 3 by applying the detailed parameters in Table 1.

From Fig. 3, it is clear that the amplitude of $G_m(s)$ increases gradually in the low-frequency range and reaches the peak at the resonant frequency (1.48×10^4 Hz). In contrast, the amplitude attenuates rapidly afterward in the high-frequency range.

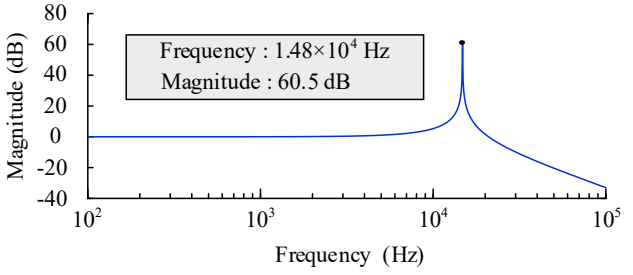

Fig. 3. Magnitude-frequency characteristic diagram of $G_m(s)$

2.3.2. External faults

The equivalent circuit of the external fault is shown in Fig. 4:

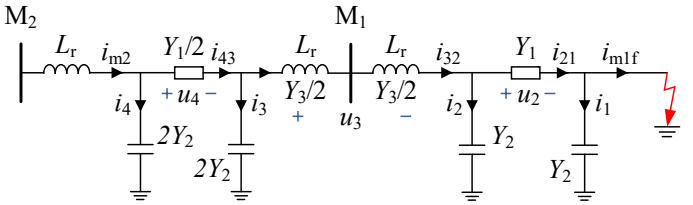

Fig. 4. Equivalent circuit of external fault

The current phasor transfer function from the fault grounding point to the M_2 terminal is defined as

$$G_{m2}(s)=\frac{\dot{I}_{m1f}(s)}{\dot{I}_{m2}(s)} \tag{7}$$

Referring to the derivation principle in the above section, the following conclusion can be drawn:

$$G_{m2}(s)=\frac{Y_1^2Y_3}{9Y_1Y_2Y_3+4Y_1^2Y_2+12Y_1Y_2^2+12Y_2^2Y_3+8Y_2^3+Y_1^2Y_3} \tag{8}$$

Then, the magnitude-frequency characteristics of $G_{m2}(s)$ are shown in Fig. 5.

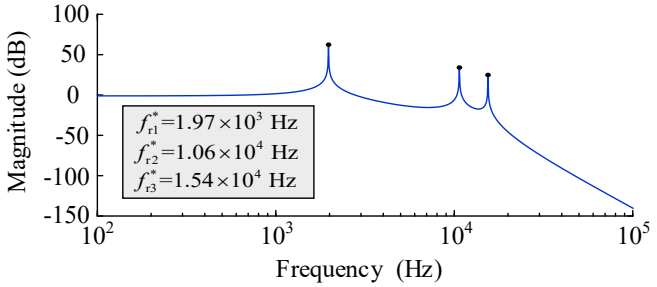

Fig. 5. Magnitude-frequency characteristic diagram of $G_{m2}(s)$

It is clear from Fig. 5 that $G_{m2}(s)$ has three resonant frequencies. In the low-frequency range, the magnitude-frequency characteristics of $G_{m2}(s)$ are similar to that of $G_m(s)$, while in the high-frequency range (over 1000 Hz), the amplitude-frequency of $G_{m2}(s)$ is significantly different from that of $G_m(s)$. There is a great difference in the frequency

characteristics between the fault and normal operating modes, distinguishing faulty feeders from normal operating ones.

2.3.3. Influence of fault resistances

Considering the influence of fault resistances on amplitude-frequency characteristics, set 10 Ω, 100 Ω and 500 Ω fault resistances respectively at the fault point. Utilize the same methods as in sections 2.3.1 and 2.3.2 for analysis and calculation, and draw the amplitude-frequency characteristic diagrams of the internal fault and external fault, as shown in Fig. 6.

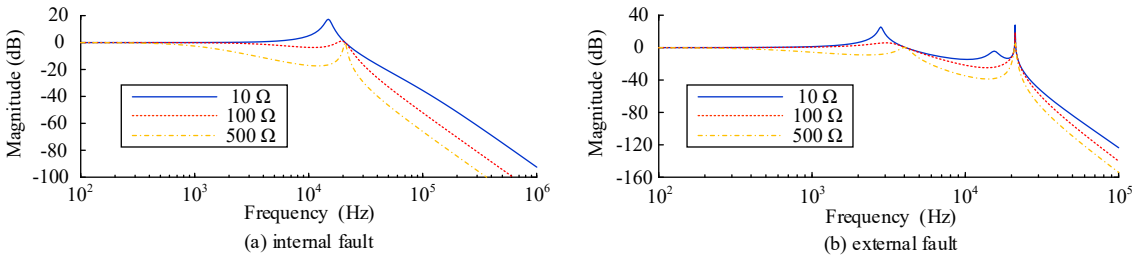

Fig. 6. Magnitude-frequency characteristic diagrams of the internal fault and external fault under the influence of fault resistances

As shown in Fig. 6, the overall trend of amplitude-frequency characteristic diagrams does not change with the increase of fault resistances. There are still great differences in the frequency band characteristics of fault transient current between the internal fault and external fault. Therefore, the amplitude-frequency characteristics of the fault transient current are not easily affected by the fault resistances and have a strong ability to withstand the fault resistances.

2.3.4. Influence of system parameters

Usually, the parameters will vary slightly in different operating scenarios with different system topologies. Therefore, it is necessary to investigate the reliability and robustness of the proposed method in the case of different system parameters. The specifications of the tested system are listed in Table 2.

Table 2. Specifications of the tested system

System parameters	S_1	S_2	S_3
R (Ω/km)	0.0139	0.1250	0.0335
L (mH/km)	0.1590	0.7200	0.3430
C (μF/km)	0.0583	0.0048	0.0021
l (km)	10	10	10
Lr (mH)	3	3	3

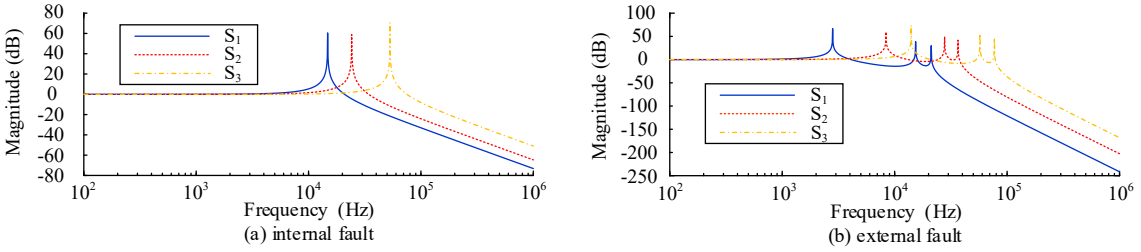

Fig. 7. Magnitude-frequency characteristic diagrams under internal and external faults

Fig. 7 shows the magnitude-frequency characteristics of the current phasor transfer function from the feeder

endpoint to the fault grounding point in three sets of parameters (S_1, S_2, S_3, see Table 2). As from Fig. 7, the magnitude-frequency characteristics stay almost unchanged, with only the magnitude of the resonance frequency greatly affected by the system parameters. Therefore, the proposed frequency-characteristic-based method is appliable to the system with varying parameters.

3. Faulty feeder detection strategy

The flowchart of the proposed method can realize the faulty feeder detection via the following two steps: protection activation and fault identification, shown in Fig. 8.

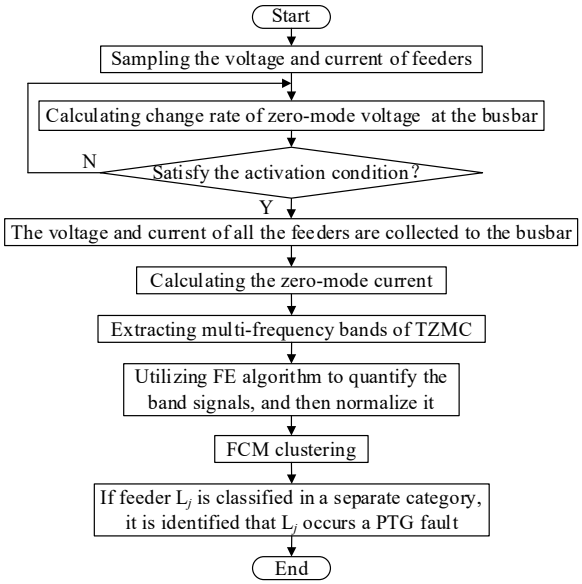

Fig. 8. The flowchart of the faulty feeder detection method

3.1. Protection activation criterion

Once a PTG fault happens in a DC transmission feeder, the positive and negative voltages will increase or decrease simultaneously, contributing to a large zero-mode component [21]. In theory, the zero-mode voltage change rate remains close to zero when the system is in normal operation, and the DC voltage fluctuations caused by load switching, power reversal, and AC faults are small [22]. By calculating the ratio of the voltage amplitude difference between the two sampling points to the sampling interval time, the change rate of zero-mode voltage is much less than that of the high resistance fault at the end of the feeder. It can ensure the reliable action of the protection under the high resistance fault at the end of the feeder. It will not make the protection misoperate in the case of non-PTG faults such as load switching, power reversal, AC fault, etc. Hence, the change rate of zero-mode voltage is applied as the protection activation criterion to activate the protection scheme in time without frequent actions. The protection activation criterion is

$$\left|\frac{\mathrm{d}(V_{\mathrm{p}}+V_{\mathrm{n}})}{\mathrm{d}t}\right| \geq V_{\mathrm{set}} \tag{9}$$

V_{p}, V_{n} is the positive and negative voltage at the busbar. V_{set} represents the activation threshold, which is less than the minimum value of the zero-mode voltage change rate under the high resistance fault at the end of the feeder as the setting principle.

3.2. Fault identification

3.2.1. Extraction of frequency bands

When a PTG fault occurs, the feeders' positive and negative voltages (and currents) require to be decoupled due to the asymmetry. The decoupling procedure is expressed in (10):

$$\begin{bmatrix} m_0 \\ m_1 \end{bmatrix} = W \begin{bmatrix} m_{\mathrm{p}} \\ m_{\mathrm{n}} \end{bmatrix} = \frac{\sqrt{2}}{2} \begin{bmatrix} 1 & 1 \\ -1 & 1 \end{bmatrix} \begin{bmatrix} m_{\mathrm{p}} \\ m_{\mathrm{n}} \end{bmatrix} \tag{10}$$

Where m_{p} and m_{n} represent feeders' positive and negative voltage (or current), W is the phase mode transformation matrix. m_0 is the zero-mode component and m_1 line-mode component. The zero-mode quantity is obtained by adding the quantities of the positive and negative electrodes. The zero-mode quantity only retains the components with the same direction in the positive and negative quantities and offsets the components with the opposite direction [22].

The zero-mode quantity is proportional to the sum of the positive and negative electrical quantities (voltage and current). The components in the same direction are added up, and the components in the opposite direction are canceled out. According to [20], the positive and negative currents of the faulty feeder flow in the same direction. Hence, the zero-mode current amplifies the transient current characteristics difference between the faulty and non-faulty feeders.

It can be seen from Section II when a PTG fault happens to the DC feeder, and there is a great difference in frequency band characteristics between the faulty feeder and non-faulty feeders. Therefore, the multi-frequency bands of TZMC can be acquired to identify the fault.

The Mallat algorithm in this paper is an efficient discrete wavelet transform technique, which includes four kinds of arithmetic operations. The calculation process is simple, reducing computational complexity and hardware operational burden. The detailed derivation of this algorithm is elaborated in (11) and (12). The process of wavelet packet decomposition is presented in Fig. 9.

$$\begin{cases} S_{2^i}^{(2q)} f(n) = \sum_{m=-1}^{2} h_m S_{2^{i-1}}^{(q)} f(n - 2^{i-1} m) \\ W_{2^i}^{(2q+1)} f(n) = \sum_{m=0}^{1} g_m S_{2^{i-1}}^{(q)} f(n - 2^{i-1} m) \end{cases} \tag{11}$$

(q is even, $i > 0$)

$$\begin{cases} S_{2^i}^{(2q)} f(n) = \sum_{m=-1}^{2} h_m W_{2^{i-1}}^{(q)} f(n - 2^{i-1} m) \\ W_{2^i}^{(2q+1)} f(n) = \sum_{m=0}^{1} g_m W_{2^{i-1}}^{(q)} f(n - 2^{i-1} m) \end{cases} \tag{12}$$

(q is odd, $i > 0$)

h_m is the low-pass filter coefficients, and g_m is the high-pass ones. $S_2^i f$ and $W_2^i f$ are the approximate and detailed components in i dimension. The derivative function of cubic B-spline is employed here as the mother wavelet function. The specific values of the filter coefficients are as shown in Table 3, given by [23].

Table 3. Coefficients of filter

Coefficients	Value	Coefficients	Value
h_{-1}	0.125	h_2	0.125
h_0	0.375	g_0	-2
h_1	0.375	g_1	2

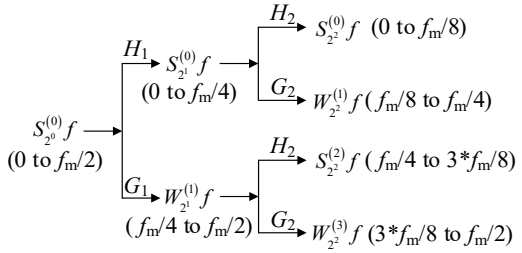

Fig. 9. Process of wavelet packet decomposition

The sampling frequency f_m of Mallat is set to be 50 kHz. Considering the requirements of rapidity and accuracy of protection, this paper divides the characteristic frequency bands into four sections. The multi-frequency bands in the second layer wavelet are extracted, and the details of the frequency bands in this paper are defined as follows: 0 to 6.25×10^3 Hz, 6.25×10^3 to 1.25×10^4 Hz, 1.25×10^4 to 1.875×10^4 Hz, and 1.875×10^4 to 2.5×10^4 Hz.

3.2.2. Construction of characteristic matrix

There is a large amount of data to be processed if all the bands are utilized to detect the faulty feeder after the frequency decomposition. Therefore, this paper introduces the fuzzy entropy (FE) algorithm to quantify the multi-frequency bands. The greater the band amplitude changes, the more complicated the waveform is, and the larger the entropy is [24].

For a V-dimensional sequence $\{x_1,x_2,\ldots,x_V\}$, a non-negative integer w is introduced to reconstruct a w-dimensional vector:

$$X_i^w = \{x(i), x(i+1), \cdots, x(i+w-1)\} - x_0(i) \quad i = 1, 2, \cdots, V-w+1 \tag{13}$$

$$x_0(i) = \frac{1}{w}\sum_{j=0}^{w-1} x(i+j) \tag{14}$$

Then, the fuzzy membership function f_x is introduced to characterize the similarity (S_{ij}^w) between X_i^w and X_j^w:

$$S_{ij} = f_x(d_{ij}^w, p, t) = \exp\{-(d_{ij})^p / t\} \tag{15}$$

Where d_{ij} represents the maximum absolute distance between X_i and X_j. p represents the fuzzy power, and t represents the tolerance.

The average similarity (φ^w) is expressed as

$$\varphi^w(V, p, t) = \frac{1}{V-w}\sum_{i=1}^{V-w}\frac{1}{V-w-1}\sum_{j=1, j\neq i}^{V-w} S_{ij} \tag{16}$$

Then, the FE can be expressed in terms of the average similarity:

$$\mathrm{FE}(V, p, t) = \lim_{V\to\infty}\{\ln\varphi^w - \ln\varphi^{w+1}\} \tag{17}$$

For a finite-length time series $\{x_1,x_2,\ldots,x_V\}$, the FE algorithm can be defined as follow:

$$\mathrm{FE}(V, p, t) = \ln\varphi^w - \ln\varphi^{w+1} \tag{18}$$

The characteristic matrix constructed by the FE algorithm is appropriate to identify the faults because it can show the difference between the information entropy of the faulty and non-faulty feeders.

3.2.3. Fuzzy C-means

Clustering is a typical unsupervised algorithm. It separates the samples into different categories to retain the similarity amongst the data in the same categories. So, the characteristic matrix can be applied for the clustering to distinguish the faulty feeder from non-faulty ones.

This paper utilizes the Fuzzy C-means (FCM) as the clustering algorithm. As the sample $X=\{x_1,x_2,\ldots x_m\}$, the clustering center is $C=\{c_1,c_2,\ldots c_n\}^{\mathrm{T}}$, and the membership matrix is $V=\{v_{ij}\}_{n\times m}$. The optimal objective function of the FCM algorithm can be written as follows:

$$\min: J_{\mathrm{FCM}}(V,C)=\sum_{i=1}^{n}\sum_{j=1}^{m}v_{ij}^{r}d_{ij}^{2}\ ,\ \text{s.t.}\ \sum_{i=1}^{n}v_{ij}=1,\ \forall j=1,2,\cdots,m \tag{19}$$

Where r represents the fuzzification coefficient. v_{ij} and d_{ij} represent the membership and the Euclidean distance of the j-th data to the i-th class, respectively.

Lagrangian multiplication is utilized to solve the minimization problem to obtain the iterative formulas of the membership and clustering center. The express is indicated in (20) and (21).

$$c_i=(\sum_{j=1}^{m}v_{ij}^{r}x_j)/(\sum_{j=1}^{m}v_{ij}^{r}) \tag{20}$$

$$v_{ij}=1/[\sum_{k=1}^{n}(\frac{d_{ij}}{d_{kj}})]^{2/(r-1)} \tag{21}$$

In the engineering application, the FCM algorithm is usually used to divide the characteristic matrix of TZMC into two categories, then obtain the membership matrix:

$$V=\begin{bmatrix} v_{11} & v_{12} & \cdots & v_{1n} \\ v_{21} & v_{22} & \cdots & v_{2n} \end{bmatrix} \tag{22}$$

Where v_{ij} represents the membership degree of category i (i=1,2) in j-th feeder, the faulty feeder can be identified because it is classified separately.

4. Simulation validations

To test the feasibility of the proposed method, a radial FDCDS is built and simulated in PSCAD/EMTDC (4.5), as displayed in Fig. 1. The solution time step of the simulation is 20.0μs. The voltage and current of each feeder are gathered at the busbar and utilized to identify the faults. The sampling frequency is set to be 50 kHz. To ensure the reliable activation of the protection under the high resistance fault at the end of the feeder, The threshold to activate the protection scheme is set to be 1 MV/s according to multiple simulation tests. The data in 3 ms is used for fault identification, consisting of 2 ms after the protection activation moment and 1 ms ahead of the protection activation moment.

Taking the positive-PTG fault in the middle of L_2 as an example, the transition resistance is set to be 0 **Ω**, and the fault occurs at the moment of 2 s. As shown in Fig. 10(a), the change rate of zero-mode voltage at the busbar exceeds the protection activation threshold instantaneously once a fault occurs. The TZMC of each feeder is shown in Fig. 10(b), which is then transformed via the Mallat wavelet algorithm into several frequency bands (see Fig. 10(c)~(f)).

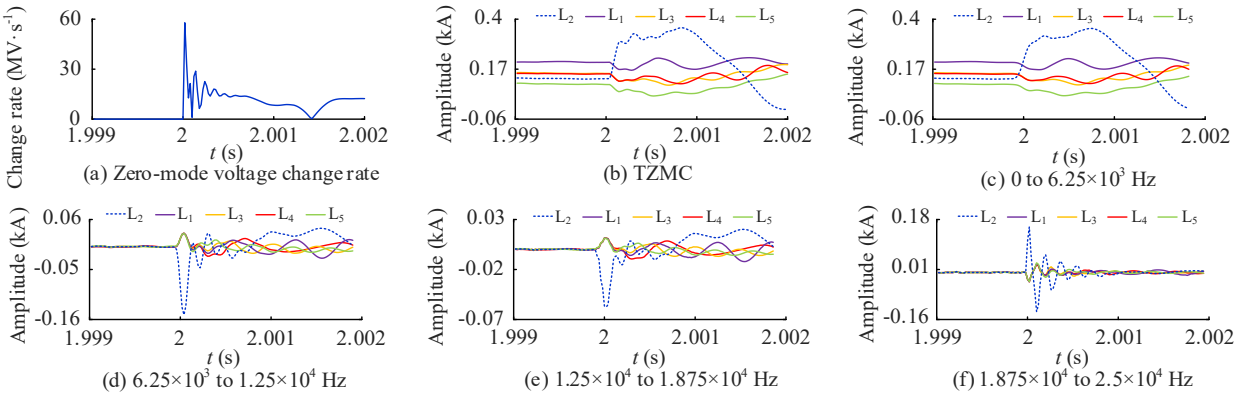

Fig. 10. Simulation results of the positive-PTG fault of L_2

As shown in Fig. 10, the amplitude variation in the faulty feeder is greater than that in the normal-operating ones so that the faulty feeder can be recognized effectively. Besides, the ripples are removed in Fig. 10(c), and the amplitude is slightly smaller in Fig. 10(c) than that in Fig. 10(b) by filtering the high-frequency components.

The characteristic matrix S is acquired by using FE in multi-frequency bands of the TZMC in each feeder:

$$S = \begin{bmatrix} 0.9419 & 0.8728 & 0.3627 & 0.9995 \\ 2.9342 & 2.1490 & 1.4091 & 1.7482 \\ 1.1958 & 1.0284 & 0.4432 & 1.0134 \\ 1.2575 & 0.9621 & 0.4206 & 1.0276 \\ 1.0648 & 1.0601 & 0.4495 & 0.9772 \end{bmatrix} \tag{23}$$

The 1st to 4th columns of the S matrix represent the features of the four characteristic band data quantized by the FE algorithm, and the 1st to 5th rows represent the features of L_1 to L_5. It can be seen that the feature of L_2 is different from other lines.

After normalization of S by column, the FCM algorithm is conducted to acquire the membership matrix V:

$$V = \begin{bmatrix} \underline{0.9938} & 0 & \underline{0.9984} & \underline{0.9963} & \underline{0.9983} \\ 0.0062 & \underline{1} & 0.0016 & 0.0037 & 0.0017 \end{bmatrix} \tag{24}$$

The 1st to 5th columns in membership matrix V represent L_1 to L_5, respectively. The largest state in each column has been underlined. As shown in (24), the largest state in the second column is in the second row, while the largest states in the rest columns are in the first row. Hence, the second row is classified as a separate category, indicating that L_2 could be a faulty feeder.

The simulation is built on PSCAD/EMTDC, and different types of faults are simulated to generate the corresponding voltage and current data. After the data is generated, it is imported into Matlab for the corresponding algorithm's operation to verify the proposed method's reliability. Note that the calculation time of Mallat, FE, and FCM in MATLAB (R2016b) is 25 μs, 1.21 ms, and 0.73 ms, respectively. Thus, it can be seen that the total running time of the above algorithms is less than 2 ms, which is rapid enough for the DC distribution networks [25].

5. Adaptability analysis

In this section, the adaptability of the proposed scheme is analyzed in 7 scenarios: different transition resistance, noises, fault positions, network topologies, sampling frequency, fault window length, and asynchronous sampling.

5.1. Influence of transition resistance

The transition resistances of positive-PTG fault in the middle of L_3 are set to be 0.1 Ω, 50 Ω, and 100 Ω here to test the robustness of the faulty feeder detection method. The simulation results shown in Table 4 indicate that the proposed method can accurately recognize the high resistance fault with strong robustness. The simulation results with 100 Ω transition resistance are displayed in Fig. 11.

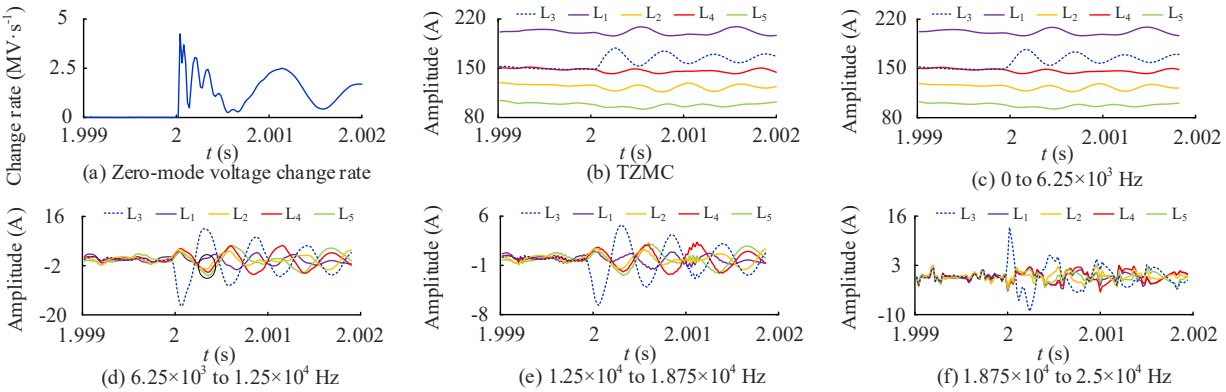

Fig. 11. Simulation results with 100 Ω transition resistance

As shown in Fig. 11, when the transition resistance is set to be 100 Ω (According to the previous publications [26]-[27], the DC fault resistance is set to be <20 Ω in the DC distribution system), the feature of fault is weak, with a certain similarity in the TZMC or its low-frequency component between the faulty and non-faulty feeders. If merely a low-frequency component is utilized to identify fault, sometimes misidentification may occur. But it is clear from Fig. 11(e) and (f) that the discrepancy of the high-frequency characteristics between faulty and non-faulty feeders are notable. Hence, the faulty feeder can be identified correctly with the combination of the high-frequency characteristics, despite the transition resistor.

Table 4. Simulation results with transition resistance

Resistance	Membership matrix V	Result
0.1 Ω	$\begin{bmatrix} \underline{0.9898} & \underline{0.9965} & 0 & 0.9988 & \underline{0.9980} \\ 0.0102 & 0.0035 & \underline{1} & 0.0012 & 0.0020 \end{bmatrix}$	Fault on L_3
50 Ω	$\begin{bmatrix} \underline{0.9979} & \underline{0.9980} & 0 & \underline{0.9919} & \underline{0.9938} \\ 0.0021 & 0.0020 & \underline{1} & 0.0081 & 0.0062 \end{bmatrix}$	Fault on L_3
100 Ω	$\begin{bmatrix} \underline{0.9428} & \underline{0.9963} & 0 & \underline{0.9880} & \underline{0.9866} \\ 0.0572 & 0.0037 & \underline{1} & 0.0120 & 0.0134 \end{bmatrix}$	Fault on L_3

5.2. Influence of noises

In industry, the noises may influence faulty feeder detection. Here, the positive-PTG fault resistance is set to be 1 Ω in the middle of L_5. The white noise is added to the original signals, with the signal-to-noise ratio (SNR) of 20 dB, 30 dB, 40 dB, and 50 dB [28]. The simulation results are listed in Table 5. The results in Table 5 show a 100% correctness rate in faulty feeder detection, demonstrating its strong disturbance rejection capability. The high-frequency noise is discarded automatically as the Mallat algorithm extracts the low-frequency band of the TZMC, which contributes to the outstanding disturbance rejection capability of this method.

Table 5. Simulation results with noises

SNR	Membership matrix V	Result
20 dB	$\begin{bmatrix} \underline{0.8296} & \underline{0.8400} & \underline{0.9908} & \underline{0.8796} & 0.0046 \\ 0.1704 & 0.1600 & 0.0092 & 0.1204 & \underline{0.9954} \end{bmatrix}$	Fault on L_5
30 dB	$\begin{bmatrix} \underline{0.9180} & \underline{0.9301} & \underline{0.9908} & \underline{0.9264} & 0.0003 \\ 0.0820 & 0.0699 & 0.0092 & 0.0736 & \underline{0.9997} \end{bmatrix}$	Fault on L_5
40 dB	$\begin{bmatrix} \underline{0.9910} & \underline{0.8751} & \underline{0.9928} & \underline{0.9878} & 0.0001 \\ 0.0090 & 0.1249 & 0.0072 & 0.0122 & \underline{0.9999} \end{bmatrix}$	Fault on L_5
50 dB	$\begin{bmatrix} \underline{0.9902} & \underline{0.8302} & \underline{0.9981} & \underline{0.9831} & 0.0004 \\ 0.0098 & 0.1698 & 0.0019 & 0.0169 & \underline{0.9996} \end{bmatrix}$	Fault on L_5

Fig. 12 displays the simulation results of the L_5 fault with SNR of 20dB. The low-frequency characteristic of the TZMC is not sensitive to the noise, which implies that the proposed method can availably avoid erroneous judgment brought by using the only high-frequency component.

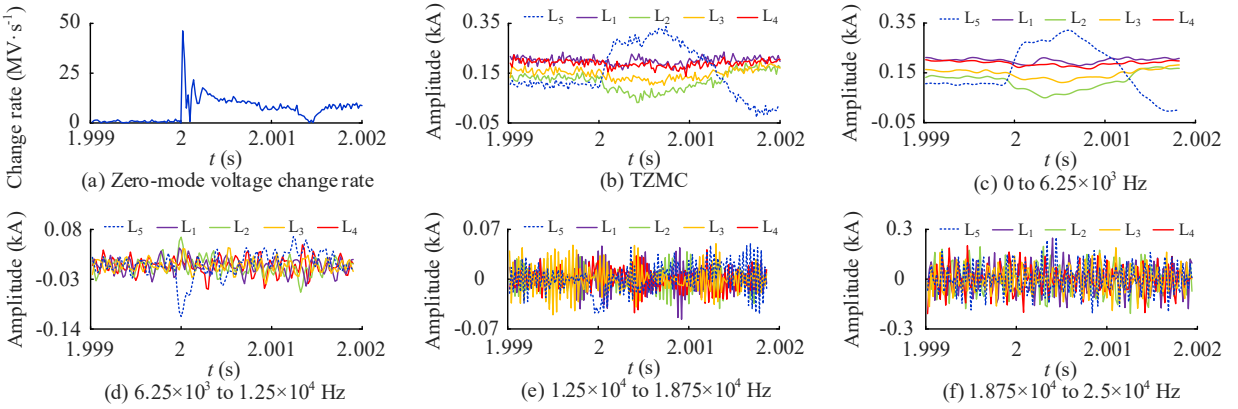

Fig. 12. Simulation results of L_5 with noise

5.3. Influence of fault positions

It is essential to consider the reliability of protection if the fault occurs in some specific positions, such as the terminals of a line. In this paper, the faults at both terminals of the feeder L_2 are generated successively to demonstrate the reliability of the protection scheme. The transition resistor is set to 30 Ω.

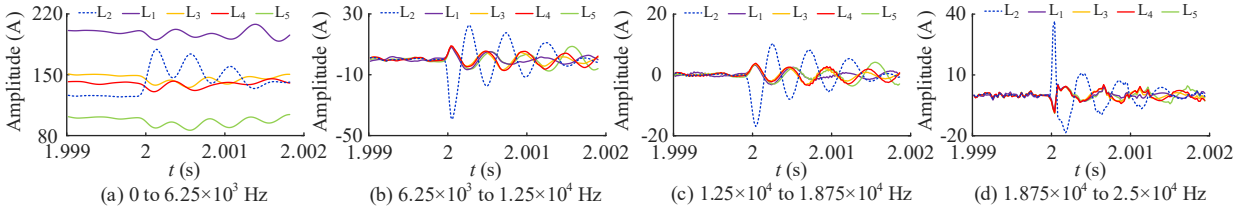

Fig. 13. Frequency band waveforms of a fault at the end of the feeder

As shown in Table 6 and Fig. 13, the proposed protection can identify the fault positions accurately. The fault is identified due to the frequency band characteristics of TZMC, which can effectively avoid the misjudgment between a fault at the end terminal of the protected feeder (internal fault) and a fault at the terminal of an adjacent feeder (external fault) to ensure the reliability of the protection scheme.

Table 6. Simulation results of extreme fault positions

Fault position	Membership matrix V	Result
Beginning	$\begin{bmatrix} \underline{0.9977} & 0 & \underline{0.9996} & \underline{0.9981} & \underline{0.9957} \\ 0.0023 & \underline{1} & 0.0004 & 0.0019 & 0.0043 \end{bmatrix}$	Fault on L_2
End	$\begin{bmatrix} \underline{0.9919} & 0 & \underline{0.9953} & \underline{0.9988} & \underline{0.9993} \\ 0.0081 & \underline{1} & 0.0047 & 0.0012 & 0.0007 \end{bmatrix}$	Fault on L_2

5.4. Influence of different network topologies

A double-terminal DC distribution system is constructed to verify the adaptability of the proposed method in different networks, as shown in Fig. 14. Here, the transition resistance of the positive-PTG fault is set to be 50 **Ω**, with the fault occurring in the middle of L_3, L_5, and L_7, respectively.

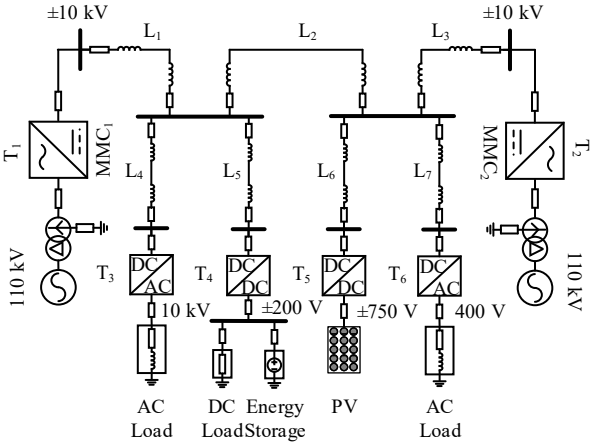

Fig. 14 The topology of double-terminal DC distribution systems

The results listed in Table 7 present strong adaptability with a 100% correctness rate in fault detection, which demonstrates its strong adaptability. Here we take a positive-PTG fault at L_7 as an example. It can be seen from Fig. 15 that the frequency band characteristics of the TZMC at the faulty feeder are different from that of the non-faulty feeder. Different network topologies do not affect the differences in frequency band characteristics between the faulty and non-faulty feeders. The protection can identify the faults in different networks effectively.

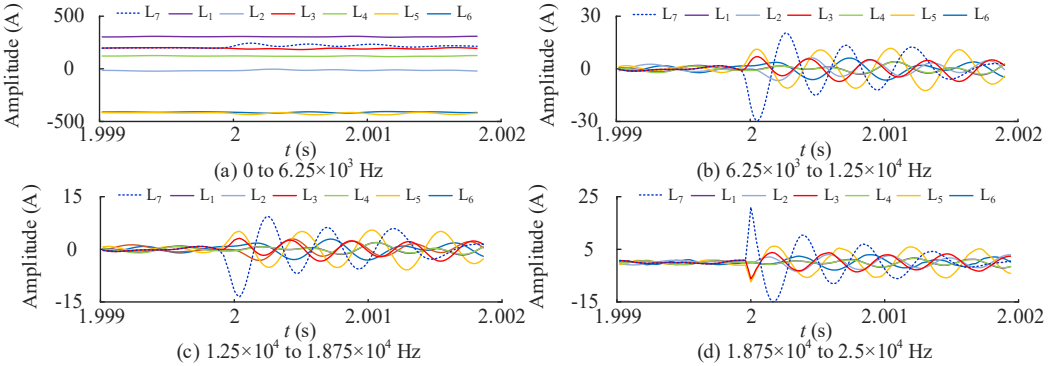

Fig. 15 Frequency band waveforms of fault in double-terminal DC distribution systems

Table 7. Simulation results of fault under double-terminal DC distribution systems

Faulty feeder	Membership matrix V	Result
L3	$\begin{bmatrix} \underline{0.9769} & \underline{0.9054} & 0.0001 & \underline{0.9706} & \underline{0.9669} & \underline{0.9840} & \underline{0.9834} \\ 0.0231 & 0.0946 & \underline{0.9999} & 0.0294 & 0.0331 & 0.0160 & 0.0166 \end{bmatrix}$	Fault on L_3
L5	$\begin{bmatrix} \underline{0.8940} & \underline{0.8879} & \underline{0.9788} & \underline{0.9561} & 0.0005 & \underline{0.9755} & \underline{0.9711} \\ 0.1060 & 0.1121 & 0.0212 & 0.0439 & \underline{0.9995} & 0.0245 & 0.0289 \end{bmatrix}$	Fault on L_5
L7	$\begin{bmatrix} \underline{0.9983} & \underline{0.9927} & \underline{0.8895} & \underline{0.9829} & \underline{0.9696} & \underline{0.9886} & 0.0001 \\ 0.0017 & 0.0073 & 0.1105 & 0.0171 & 0.0304 & 0.0114 & \underline{0.9999} \end{bmatrix}$	Fault on L_7

5.5. Influence of sampling frequency

In industry, the sampling frequency is often adjusted according to the actual situation, so the sampling frequency of different systems is not the same. Verifying the adaptability to the sampling frequency becomes necessary. Here, the transition resistance of the positive-PTG fault is set to be 20 Ω with the fault occurring in the middle of L_5, and the sampling frequency is set to be 25 kHz, 50 kHz, and 100 kHz, respectively. The simulation results are shown in Table 8.

Table 8. Simulation results of different sampling frequency

Sampling frequency	Membership matrix V	Result
25 kHz	$\begin{bmatrix} \underline{0.9931} & \underline{0.9991} & \underline{0.9979} & \underline{0.9996} & 0 \\ 0.0069 & 0.0009 & 0.0021 & 0.0004 & \underline{1} \end{bmatrix}$	Fault on L_5
50 kHz	$\begin{bmatrix} \underline{0.9957} & \underline{0.9996} & \underline{0.9999} & \underline{0.9984} & 0 \\ 0.0043 & 0.0004 & 0.0001 & 0.0016 & \underline{1} \end{bmatrix}$	Fault on L_5
100 kHz	$\begin{bmatrix} \underline{0.9948} & \underline{0.9994} & \underline{0.9987} & \underline{0.9751} & 0 \\ 0.0052 & 0.0006 & 0.0013 & 0.0249 & \underline{1} \end{bmatrix}$	Fault on L_5

The influence of sampling frequency is analyzed with the frequency band set to be 6.25×10^3 to 1.25×10^4 Hz. As shown in Fig. 16, the frequency band characteristics between internal and external faults are significantly different in the case of various sampling frequencies, which means the protection criterion of the proposed method will not be influenced by the sampling frequency.

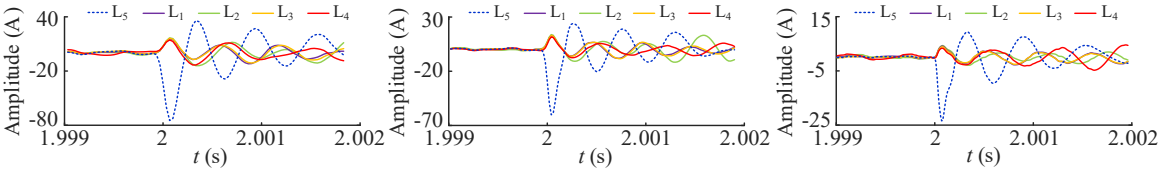

(a) Sampling frequency under 25 kHz (b) Sampling frequency under 50 kHz (c) Sampling frequency under 100 kHz

Fig. 16 Frequency bands of 6.25×103 to 1.25×104 Hz

5.6. Influence of fault window length

There is a transition process when PTG fault occurs due to the influence of load current. When the operating state changes from normal to a fault, the protection will not start up immediately. Especially when the system sampling frequency is high and the fault window length is short, the protection is usually unable to meet DC line protection's reliability and speed requirements. Therefore, it is of great necessity to investigate the influence of fault window length.

Table 9 shows the identification results of positive-PTG fault when the fault window length is 0.5 ms, 1.0 ms, and

1.5 ms. The fault occurred in the middle of L_4, and the transition resistance is 100 Ω. Note that the previous length of the fault data window is 1 ms.

Table 9. Simulation results with different fault window length

Fault window length	Membership matrix V	Result
0.5 ms	$\begin{bmatrix} \underline{0.9136} & \underline{0.9994} & \underline{0.9851} & 0.0008 & \underline{0.9798} \\ 0.0864 & 0.0006 & 0.0149 & \underline{0.9992} & 0.0202 \end{bmatrix}$	Fault on L_4
1.0 ms	$\begin{bmatrix} \underline{0.9217} & \underline{0.9971} & \underline{0.9939} & 0 & \underline{0.9919} \\ 0.0783 & 0.0029 & 0.0061 & \underline{1} & 0.0081 \end{bmatrix}$	Fault on L_4
1.5 ms	$\begin{bmatrix} \underline{0.9933} & \underline{0.9993} & \underline{0.9989} & 0 & \underline{0.9945} \\ 0.0067 & 0.0007 & 0.0011 & \underline{1} & 0.0055 \end{bmatrix}$	Fault on L_4

As shown in Table 9, the protection is reliable with a short fault data window length of 0.5 ms. Therefore, the protection scheme proposed in this paper is not affected by the change of data window length. Fig. 17 shows the TZMC in different frequency bands with a fault data window length of 0.5 ms, which shows the distinguished fault characteristics. The fault identification results are reliable and accurate in short data window length.

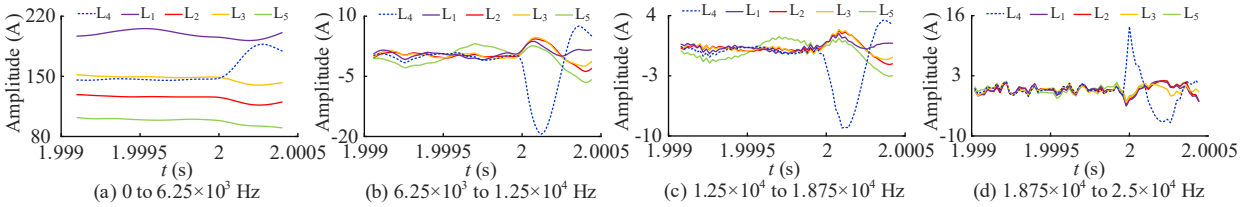

(a) 0 to 6.25×10^3 Hz (b) 6.25×10^3 to 1.25×10^4 Hz (c) 1.25×10^4 to 1.875×10^4 Hz (d) 1.875×10^4 to 2.5×10^4 Hz

Fig. 17. Frequency band waveforms of 0.5 ms fault window length

5.7. Influence of asynchronous sampling

As the proposed method needs the current of all the feeders to detect the faulty feeder, the asynchronous sampling may negatively influence the recognition results. To check this influence, this paper considers the sampling on L_3 and L_4 lag that on L_1 10 sampling points and L_5 lags L_1 16 sampling points. Positive-PTG faults are generated in L_1, L_3, and L_5 with transition resistance of 10 Ω. The recognition result is shown in Table 10. It demonstrates the strong reliability of the proposed method, which gets little impact from the asynchronous sampling.

Table 10. Simulation results with asynchronous sampling

Faulty feeder	Membership matrix V	Result
L_1	$\begin{bmatrix} 0.0022 & \underline{0.8740} & \underline{0.9460} & \underline{0.9113} & \underline{0.9516} \\ \underline{0.9978} & 0.1260 & 0.0540 & 0.0887 & 0.0484 \end{bmatrix}$	Fault on L_1
L_3	$\begin{bmatrix} \underline{0.9621} & \underline{0.8621} & 0.0003 & \underline{0.9665} & \underline{0.9899} \\ 0.0379 & 0.1379 & \underline{0.9997} & 0.0335 & 0.0101 \end{bmatrix}$	Fault on L_3
L_5	$\begin{bmatrix} \underline{0.9627} & \underline{0.8429} & \underline{0.9312} & \underline{0.8437} & 0.0017 \\ 0.0373 & 0.1571 & 0.0688 & 0.1563 & \underline{0.9983} \end{bmatrix}$	Fault on L_5

6. Accuracy analysis

Table 11. Details of samples

Transition resistance (Ω)	SNR (dB)	Fault positions	Sampling frequency (kHz)	Total numbers
0.1, 10, 50, 100	20, 30, 40, 50	Middle of L_2, End of L_2	25, 50, 100	96

As shown in Table 11, Ninety-four fault conditions have been tested in this paper. Ninety-four fault conditions can be accurately identified, and the accuracy is as high as 98%. By analyzing the misjudged faults, it can be found that they occur in the extreme cases of high resistance grounding fault at the end of the feeder and are accompanied by strong noise. However, for the vast majority of fault conditions, the method proposed in this paper has strong reliability.

7. Comparison with the existing methods

The results of the proposed method are compared to three typical fault detection methods, which are based on current high-frequency transient energy (HFE) [29], the fault components correlation (FCC) of the positive & negative currents [18], and the transient current derivative (TCD)[30].

The PTG fault resistance is 1 Ω or 100 Ω in the middle of L_2. It can be seen from Table 12 that all the methods provide misidentified results when the transition resistance is 100Ω. It is due to the unclear fault boundary of DC distribution systems, the high similarity in fault phenomenon between the large internal and small external resistance, and the fluctuation of distributed capacitor current under the PTG fault. It is difficult to realize accurate fault feeder identification by merely utilizing a single frequency band or signal correlation or set threshold, which has been solved by the proposed method.

Table 12. Simulation Results of the Existing Methods

Method	Resistance	Criteria matrix: $[L_1 \quad L_2 \quad L_3 \quad L_4 \quad L_5]$
HFE	1 Ω	[0.0514 1.4128 0.0583 0.1350 0.0769]
	100 Ω	[0.0076 0.0731 0.0071 0.0068 0.0094]
FCC	1 Ω	[0.9749 –0.7614 0.9824 0.9662 0.9820]
	100 Ω	[0.9573 0.8543 0.8481 0.9944 0.8380]
TCD	1 Ω	[–0.0058 0.0073 0.0030 –0.0070 0.0029]
	100 Ω	[–0.0011 0.0026 –0.0006 –0.0015 –0.0006]

8. Conclusion

In this paper, a PTG fault feeder detection method for radial FDCDSs was presented based on the multi-frequency bands characteristic of the TZMC. Based on the findings of the proposed work, the following can be concluded：

1) Through theoretical analysis and simulation verification, it is proved that there are differences in frequency domain characteristics of TZMC under internal and external faults, and those frequency domain characteristics are not affected by system parameters and transition resistance.

2) The utilization of TZMC multi-frequency bands characteristic improved the disturbance rejection capability of the protection scheme and avoided the misidentification caused by using fixed bands. The fault feeder detection was achieved using the FCM clustering, which avoided the complicated threshold setting and calculation. In addition, training data was not required for this algorithm, which solved the problem of insufficient on-site data in industrial applications.

3) Simulation results show that the method has 98% accuracy in the 96 samples tested. This method can adapt to 100 Ω transition resistance, the signal-to-noise ratio of 20 dB, fault location change, system topology change, sampling frequency change, fault window length change, and asynchronous sampling. It has excellent robustness, which is more applicable in engineering applications.

4) Compared to typical methods, such as HFE, FCC, and TCD, the proposed method has advantages over the capability of faulty feeder detection, the robustness to high resistance, and noise disturbance.

Acknowledgements

The authors gratefully acknowledge the financial support from the National Natural Science Foundation of China (NSFC) under Project Numbers 51677030.

Appendix

The structure and parameters of the DC cables in this paper are shown in Fig. 18.

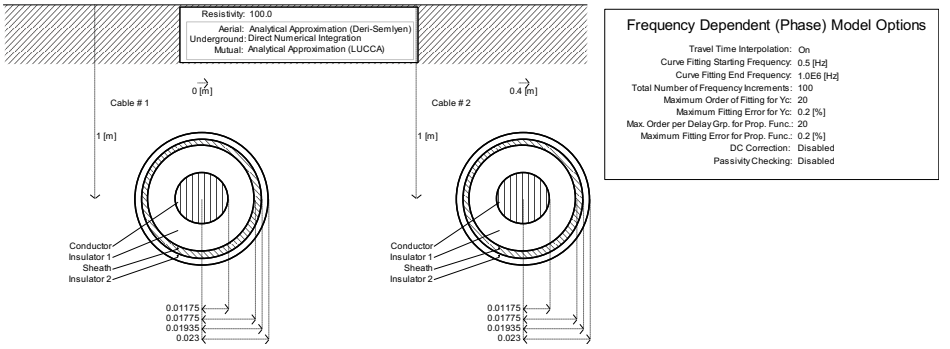

Fig. 18. Implemented cable line configuration

References

[1] Wang Y, Li Q, Li B, Wei T, Zhu Z, Li W, Wen W, Wang C. A practical DC fault ride-through method for MMC based MVDC distribution systems. *IEEE Transactions on Power Delivery* 2021;36(4);2510-19.

[2] Zheng T, Lv W, Wu Q, Li R, Liu X, Zhang C, Xu L. An integrated control and protection scheme based on FBSM-MMC active current limiting strategy for DC distribution network. *IEEE Journal of Emerging and Selected Topics in Power Electronics* 2021;9(3);2632-42.

[3] Feng XY, Qi L, Pan JP. A novel fault location method and algorithm for DC distribution protection. *IEEE Transactions on Industry Applications* 2017;53(3):1834-40.

[4] Xue SM, Lian J, Qi JL, Fan BY. Pole-to-ground fault analysis and fast protection scheme for HVDC based on overhead transmission lines. *Energies* 2017;10(7):1059-75.

[5] Yu JQ, Zhang ZR, Xu Z, Wang GT. An equivalent calculation method for pole-to-ground fault transient characteristics of symmetrical monopolar MMC based DC grid. *IEEE Access* 2020;8:123952-65.

[6] He S, Zou GB, Sun CJ, Liu SM. Fault section locating method and recovery strategy of pole-to-ground fault for medium voltage direct current (MVDC) distribution network. *The Journal of Engineering*, vol 2019;16:668-73.

[7] Li BT, Ren X, Li B. Study on the charge transfer criterion for the pole-to-ground fault in DC distribution networks. *IEEE Access* 2019;7:102386-96.

[8] Jia YY, Gao S, Si XY, Shi Y, Zhan X, Wang JH. Protection method of flexible DC power distribution network based on grounding mode with high resistor and arrester in parallel. *Automation of Electric Power Systems* 2020;44(10):166-73.

[9] Wang CB, Jia K, Bi TS, Xuan ZW, Zhu R. Transient current curvature based protection for multi-terminal flexible dc distribution systems. *IET Generation, Transmission & Distribution* 2019;13(15):3484-92.

[10] Jia K, Wang CB, Bi TS, Zhu R, Xuan ZW. Transient current waveform similarity based protection for flexible DC distribution system. *IEEE Transactions on Industrial Electronics* 2019;66(12):9301-11.

[11] Zhang XP, Tai NL, Fan CJ, Zheng XD, Huang WT. Fault line selection in DC distribution network based on VPC-EMTR theory. *High Voltage Engineering* 2020;46(5):1729-39.

[12] Yang S, Xiang W, Li R, Lu X, Zuo W, Wen J. An improved DC fault protection algorithm for MMC HVDC grids based on modal-domain analysis. *IEEE Journal of Emerging and Selected Topics in Power Electronics* 2020;8(4):4086–99.

[13] Wang X, Song G, Gao J, Wei X, Wei Y, Mostafa K, Hu Z, Zhang Z. High impedance fault detection method based on improved complete ensemble empirical mode decomposition for DC distribution network. *Electrical Power and Energy Systems* 2019;107:538-556.

[14] Luo GM, Yao CY, Liu YL, Tan YJ, He JH, Wang K. Stacked auto-encoder based fault location in VSC-HVDC. *IEEE Access* 2018;6:33216-24.

[15] Tiwari SP, Koley E, Ghosh S. Communication-less ensemble classifier-based protection scheme for DC microgrid with adaptiveness to network reconfiguration and weather intermittency. *Electric Power Systems Research* 2021;26:100460.

[16] Farshad M, Karimi M. Intelligent protection of CSC-HVDC lines based on moving average and maximum coordinate difference criteria. *Electric Power Systems Research* 2021;199:107439.

[17] Hossam-Eldin A, Lotfy A, Elgamal M, Ebeed M. Artificial intelligence-based short-circuit fault identifier for MT-HVDC systems. *IET*

Generation, Transmission & Distribution 2018;12(10):2436-43.
[18] Zeng Y, Zou GB, Zhang X, Wei XY, Jiang LT, Sun CJ. Faulty feeder selection and segment location method for SPTG fault in radial MMC-MVDC distribution grid. *IET Generation, Transmission & Distribution* 2020;14(2):223-33.
[19] Liu G, Zhao Y, Yuan Z, et al. Study on demonstration project technical scheme of VSC-DC distribution system in Shenzhen. *Southern Power System Technology* 2016;10(4);1-7.
[20] Bi TS, Wang S, Jia K, Zhou ZX, Li W. Short-term energy based approach for monopolar grounding line identification in MMC-MTDC System. *Power System Technology* 2016;40(3):689-95.
[21] Nougain V, Mishra S, Misyris G S, Chatzivasileiadis S. Multiterminal DC fault identification for MMC-HVDC systems based on modal analysis—a localized protection scheme. *IEEE Journal of Emerging and Selected Topics in Power Electronics* 2021;9(6);6650-61.
[22] Xiang W, Yang SZ, Xu L, Zhang JJ, Lin WX, Wen JY. A transient voltage-based DC fault line protection scheme for MMC-based DC grid embedding DC breakers. *IEEE Transactions on Power Delivery* 2019;34(1):334-45.
[23] Lin C, Gao W, Guo MF. Discrete wavelet transform-based triggering method for single-phase earth fault in power distribution systems. *IEEE Transactions on Power Delivery* 2019;34(5):2058-68.
[24] Wang BP, Ma JJ, Han ZX, Zhang Y, Fang Y, Ge YM. Adaptive image enhancement algorithm based on fuzzy entropy and human visual characteristics. *Journal of Systems Engineering and Electronics* 2018;29(5):1079-88.
[25] Jia K, Xuan ZW, Feng T, Wang CB, Bi TS, Thomas DWP. Transient high-frequency impedance comparison-based protection for flexible DC distribution systems. *IEEE Transactions on Smart Grid* 2020;11(1):323-33.
[26] Yang J, Fletcher J E, O'Reilly J. Short-Circuit and gound fault analyses and location in VSC-based DC network cables. *IEEE Transactions on Industrial Electronics*, vol 2012;59(10):3827-37.
[27] Satpathi K, Yeap Y M, Ukil A, Geddada N. Short-time Fourier transform based transient analysis of VSC interfaced point-to-point DC system. *IEEE Transactions on Industrial Electronics* 2018;65(5):4080–91.
[28] Carrica D, Benedetti M, Petrocelli R. Random sampling applied to the measurement of a DC signal immersed in noise. *IEEE Trans. Instrum. Meas* 2001;50(5):1319–23.
[29] Li YJ, Wu L, Li JP, Xiong LS, Zhang X, Song G, Xu Z. DC fault detection in MTDC systems based on transient high frequency of current. *IEEE Transactions on Power Delivery* 2019;34(3):950-62.
[30] Meghwani A, Srivastava S C, Chakrabarti S. A non-unit protection scheme for DC microgrid based on local measurements. *IEEE Transactions on Power Delivery* 2017;32(1):172–81.